Biochemistry **2003,** *42,* 13269−13279

Structural Characterization of the Peroxodiiron(III) Intermediate Generated during Oxygen Activation by the W48A/D84E Variant of Ribonucleotide Reductase Protein R2 from *Escherichia coli*[†]

Jeffrey Baldwin,[‡] Carsten Krebs,[§,||] Lana Saleh,[‡] Mindy Stelling,[⊥] Boi Hanh Huynh,[§] J. Martin Bollinger, Jr.,[‡] and Pamela Riggs-Gelasco*[,⊥]

Department of Biochemistry and Molecular Biology, The Pennsylvania State University, University Park, Pennsylvania 16802, Department of Physics, Emory University, Atlanta, Georgia 30322, and Department of Chemistry and Biochemistry, College of Charleston, 66 George Street, Charleston, South Carolina 29424

Received July 9, 2003; Revised Manuscript Received September 10, 2003

ABSTRACT: The diiron(II) cluster in the R2 subunit of *Escherichia coli* ribonucleotide reductase (RNR) activates oxygen to generate a μ-oxodiiron(III) cluster and the stable tyrosyl radical that is critical for the conversion of ribonucleotides to deoxyribonucleotides. Like those in other diiron carboxylate proteins, such as methane monooxygenase (MMO), the R2 diiron cluster is proposed to activate oxygen by formation of a peroxodiiron(III) intermediate followed by an oxidizing high-valent cluster. Substitution of key active site residues results in perturbations of the normal oxygen activation pathway. Variants in which the active site ligand, aspartate (D) 84, is changed to glutamate (E) are capable of accumulating a μ-peroxodiiron(III) complex in the reaction pathway. Using rapid freeze−quench techniques, this intermediate in a double variant, R2-W48A/D84E, was trapped for characterization by Mössbauer and X-ray absorption spectroscopy. These samples contained 70% peroxodiiron(III) intermediate and 30% diferrous R2. An Fe−Fe distance of 2.5 Å was found to be associated with the peroxo intermediate. As has been proposed for the structures of the higher valent intermediates in both R2 and MMO, carboxylate shifts to a μ-(η^1,η^2) or a μ-1,1 conformation would most likely be required to accommodate the short 2.5 Å Fe−Fe distance. In addition, the diferrous form of the enzyme present in the reacted sample has a longer Fe−Fe distance (3.5 Å) than does a sample of anaerobically prepared diferrous R2 (3.4 Å). Possible explanations for this difference in detected Fe−Fe distance include an O_2-induced conformational change prior to covalent chemistry or differing O_2 reactivity among multiple diiron(II) forms of the cluster.

Ribonucleotide reductase (RNR)[1] catalyzes the conversion of ribonucleotides to deoxyribonucleotides, a reaction critical for DNA synthesis. The class I RNRs have an $\alpha_2\beta_2$ structure, where the α subunit, R1, contains the nucleotide binding site and the five conserved cysteine residues that participate in substrate reduction (*1*, *2*). The β subunit, R2, contains a μ-oxodiiron(III) cluster and an adjacent stable tyrosyl radical at position 122 (*Escherichia coli*) (*3*). The tyrosyl radical is thought to generate a thiyl radical on the R1 subunit via long-range electron/proton transfer through a network of conserved residues contributed by both R1 and R2 (*4*−*8*).

The R2 cofactor spontaneously self-assembles from the apoprotein, Fe(II), and O_2 (*9*). The first intermediate to be identified in the self-assembly reaction is the Fe(III)/Fe(IV) cluster known as X. X can oxidize Y122 to Y122$^\bullet$ and can be trapped cryogenically by spraying a reaction mixture into cold (<−140 °C) liquid isopentane. By using this rapid freeze−quench (RFQ) technique, samples of X have been prepared for characterization by Mössbauer (*10*, *11*), ENDOR (*12*−*15*), EPR (*16*), and EXAFS (*17*) spectroscopies. The EXAFS spectra of samples containing ≈40% diferrous R2 and 60% X have prominent features at 2.5 Å and short Fe−O interactions, which are best modeled as Fe−Fe vectors and

---

[†] This work was supported by NIH-South Carolina BRIN Grant 1 P20 RR16461-01 (P.R.-G.), by NIH Grants GM55365 (J.M.B.) and GM58778 (B.H.H.), and by a Camille and Henry Dreyfus Foundation Faculty Start-up Grant for Undergraduate Institutions (P.R.-G.). Portions of this research were carried out at the Stanford Synchrotron Radiation Laboratory, a national user facility operated by Stanford University on behalf of the U.S. Department of Energy, Office of Basic Energy Sciences. The SSRL Structural Molecular Biology Program is supported by the Department of Energy, Office of Biological and Environmental Research, and by the National Institutes of Health, National Center for Research Resources, Biomedical Technology Program.

* To whom correspondence should be addressed. E-mail: gelascop@cofc.edu. Tel: (843) 953-7182. Fax: (843) 953-1404.

[‡] The Pennsylvania State University.

[§] Emory University.

[||] Present address: Department of Biochemistry and Molecular Biology, The Pennsylvania State University, University Park, PA 16802.

[⊥] College of Charleston.

[1] Abbreviations: bp, base pairs; CN, coordination number; Δ^9-desaturase, stearoyl acyl carrier protein Δ^9 desaturase; ENDOR, electron−nuclear double resonance spectroscopy; EPR, electron paramagnetic resonance; EXAFS, extended X-ray absorption fine structure spectroscopy; FT, Fourier transform; HEPES, *N*-(2-hydroxyethyl)-piperazine-*N*′-2-ethanesulfonic acid; HB(pz′)$_3$, hydrotris(3,5-diisopropyl-1-pyrazolyl)borate; 6-Me$_3$-TPA, tris(6-methyl-2-pyridylmethyl)amine; MMO, methane monooxygenase; OBz, benzoate; R2$_{\text{peroxo}}$, the peroxodiiron(III) species that accumulates during oxygen activation by D84E variants of R2; RFQ, rapid freeze−quench; RNR, ribonucleotide reductase; XAS, X-ray absorption spectroscopy; Y122$^\bullet$, free radical form of tyrosine 122.

10.1021/bi035198p CCC: $25.00

Scheme 1

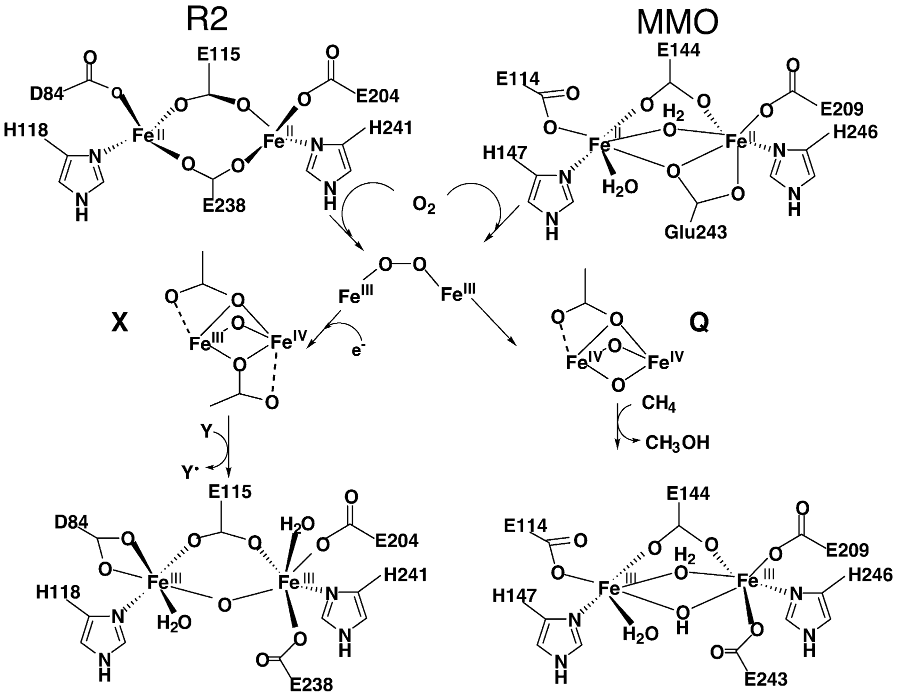

Fe−μ-oxo interactions, respectively (*17*). When these structural constraints were considered with $^{17}O_2$ and $H_2{}^{17}O$ ENDOR data on X, the structure shown in Scheme 1 was proposed (*13*, *17*). The short Fe−Fe distance requires three single-atom bridges. Since the ENDOR data on X indicate that only one oxygen atom from O_2 bridges the Fe(III)/Fe(IV) pair (*13*), the other two bridges are most likely single oxygens from carboxylate ligands E115 and E238. Both of these residues are μ-(1,3) bridges in published structures of diiron(II) R2, but an O_2-derived oxo bridge displaces E238 from Fe1 in the product diiron(III) form (*4*, *18*). Such “carboxylate shifts” (*19*) are common structural rearrangements in R2 and other diiron carboxylate proteins such as the hydroxylase component of methane monoxygenase (MMO) and stearoyl acyl carrier protein Δ^9-desaturase (*18*, *20*−*23*). Indeed, a μ-(η^1,η^2) coordination mode (with one carboxylate oxygen bridging and one coordinated only to Fe2) has been observed for E238 in several structures of diiron(II) forms of R2 variants (*24*, *25*) and for the corresponding residue, E243, in diiron(II) MMO (*22*).

The R2 iron cluster activates oxygen for a one-electron oxidation of Y122 to Y122• in a stoichiometric reaction, while MMO catalytically activates oxygen for the two-electron oxidation of methane to methanol. Two Fe−oxygen intermediates in the MMO oxygen activation reaction have been extensively characterized, P (or H_{peroxo}) and Q (Scheme 1) (*26*−*29*). The peroxodiiron(III) species, P, converts without change in its net redox state to Q, an antiferromagnetically coupled Fe(IV)/Fe(IV) dimer that also has a 2.5 Å Fe−Fe distance (*30*). A mixed valent intermediate can be cryogenically generated by radiolytic reduction of Q to Q_X, an Fe(III)/Fe(IV) cluster having spectroscopic properties similar to those of species X in R2 (*31*).

It has frequently been proposed that the pathway of O_2 activation in R2 is similar to that in MMO and includes peroxodiiron(III) and diiron(IV) intermediates similar or identical to P and Q, respectively (*29*, *32*, *33*). Some optical and Mössbauer spectroscopic evidence for a very short lived peroxodiiron(III) species (*34*) has been presented, but a recent kinetic study is inconsistent with the accumulation of an intermediate between the diiron(II) reactant and cluster X (*35*). No evidence for a Q-like species has yet been obtained, perhaps because one-electron reductive cleavage of the putative peroxodiiron(III) species leads directly to X. Thus, at present, the point at which the mechanisms of the MMO and R2 reactions diverge, either very early with formation of different initial diiron(II)−O_2 adducts or later with distinct pathways for decay of a common intermediate, is not known.

As shown in Scheme 1, the protein ligands coordinating the diiron active sites are $(His)_2(carboxylate)_4$ for both MMO and R2 (*22*, *23*). There is but one nonidentity among these ligands: the MMO ligand corresponding to aspartate 84 in R2 is a glutamate (E114). Bollinger et al. found that R2 variants with this aspartate ligand changed to glutamate (R2-D84E, R2-W48F/D84E, R2-W48A/D84E) are, in contrast to the wild-type protein, capable of accumulating a peroxodiiron(III) intermediate ($R2_{peroxo}$) during O_2 activation (*36*). By use of the rapid freeze−quench (RFQ) method to trap the diamagnetic $R2_{peroxo}$, the Mössbauer properties of this intermediate were determined ($\delta = 0.63$ mm/s and $\Delta E_Q = 1.58$ mm/s) and were found to be very similar to those of P in MMO ($\delta = 0.66$ mm/s and $\Delta E_Q = 1.51$ mm/s). $R2_{peroxo}$ also has a broad absorption feature at 700 nm very similar to those of P and synthetic peroxodiiron(III) species (*26*, *37*, *38*). In R2-D84E, the disappearance of the 700 nm feature and the Mössbauer quadrupole doublet of the peroxo intermediate is kinetically correlated with formation of the tyrosyl radical. Both the O−O and the Fe−O_2 stretching frequencies were identified in the resonance Raman spectra of the intermediate, leading to the conclusion that the peroxide ligand is a symmetric μ-1,2 bridge (*39*). Substitution of tryptophan 48 with phenylalanine was found to increase the lifetime of the complex by approximately 4-fold (*39*, *40*), consistent with the hypothesis that the peroxo complex may undergo direct reduction by this residue (*35*, *41*−*43*). In later work, it was shown that the intermediate can be trapped with 70% of the Fe in the peroxo oxidation state in the R2-W48A/D84E variant. In this paper, the greater homogeneity of the complex achieved with this variant has been exploited, and X-ray absorption spectroscopy has been used to define key structural constraints on the peroxo intermediate that accumulates in variants of R2 with the D84E substitution.

MATERIALS AND METHODS

Preparation of the Expression Vector for R2-W48A/D84E. The W48G substitution was introduced into the *nrdB* gene (encoding R2) by using the polymerase chain reaction (PCR) and the previously described plasmid, pR2-W48F (*44*), as template. Primers 1 (5′-GAA GTG GCG AGC CCG ATC TTC CCC-3′) and 2 (5′-GGG A*GA CGT C*AA CCT CCT CCG GCC G**AC C**GA AGA AAG AGA GC-3′) were used to amplify a 392 base pair (bp) fragment. Primer 1 anneals ∼115 bp 5′ of a unique *Bgl*II site, which is 105 bp 5′ of the start of *nrdB* in pR2-W48F. Primer 2 introduces a unique *Eag*I restriction site (underlined) and the desired W48G substitution at codon W48 (TGG to GGT, complement of boldface triplet) and also spans the unique *Aat*II restriction site (underlined and italicized) in codon V55 of *nrdB*. The PCR fragment was digested with *Bgl*II and *Aat*II and ligated with the large fragment generated by digestion of pR2-W48F with the same enzymes, yielding pR2-W48G. The *Eag*I restriction site introduced in pR2-W48G was exploited to prepare the pR2-W48A plasmid. Primers 1 and 3 (5′-CTC CTC CGG CCG **CGC** GAA GAA AGA GAG C-3′) were used to generate a 379 bp PCR fragment consisting of nucleotides 1−159 of the coding sequence, 105 nucleotides of the vector sequence upstream of the start codon (3′ of the *Bgl*II restriction site), and 115 additional nucleotides 5′ of the *Bgl*II site. Primer 3 introduces the desired G48 to alanine substitution (TGG to GCG, complement of boldface triplet). The PCR product was digested with *Bgl*II and *Eag*I and then ligated with the large fragment from digestion of pR2-W48G with the same enzymes. To construct pR2-W48A/D84E, the 268 bp *Bgl*II to *Aat*II restriction fragment (containing codons 1−52) from pR2-W48A was joined with the large fragment from digestion of pR2-D84E [previously described (*39*)] with the same enzymes. The sequence of the coding regions of each plasmid construct was verified to ensure that no undesired mutations had been introduced. The Nucleic Acid Facility of the The Pennsylvania State University Biotechnology Institute sequenced the DNA.

Overexpression and Purification of Tryptophan 48 Variant Proteins. Successful overexpression and purification of R2 variants containing the W48A or W48G (W48X) substitution required modifications to the existing protocol (*44*). Inclusion of 10% [weight/volume (w/v)] glycerol in the culture medium and buffers used in purification was found to enhance both the yield and quality [purity and quantity of Fe(II) incorporated] of W48X variants. *E. coli* strain BL21(DE3) transformed with the appropriate plasmid was grown with vigorous aeration at 37 °C in enriched medium containing 10% glycerol (w/v) and 150 μg/mL ampicillin. Details of the fermentation protocol have been described (*41*). The yield was approximately 20 g of cell paste/L of medium. In a typical purification, 60 g of the frozen cell paste was thawed and resuspended at 4 °C in 300 mL of buffer A [50 mM Tris, pH 7.6, 10% (w/v) glycerol] containing 0.25 mM PMSF and 1 mM 1,10-phenanthroline. Cell lysis and streptomycin precipitation steps were carried out as previously described (*41*). An additional ammonium sulfate precipitation step, in which the solution was brought to 30% of saturation and the supernatant was recovered, was performed prior to the 60% (of saturation) ammonium sulfate fractionation step used in earlier protocols (*44*−*46*). The pellet from the latter step was redissolved in buffer A (1 mL/g of wet cell mass) containing 0.25 mM PMSF and 1 mM 1,10-phenanthroline, and this solution was dialyzed for 4 h against 6 L of buffer A. An equal volume of buffer A containing 0.25 mM PMSF was added to the dialysate, and the solution was loaded on a 5 cm × 40 cm (0.8 L) Q-Sepharose fast-flow (Pharmacia) column equilibrated in buffer A. The column was washed with 0.3 L of buffer A, followed by 1 L of buffer A containing 225 mM NaCl. The protein was eluted with buffer A containing 300 mM NaCl. Fractions containing protein (as judged by their light absorption spectra) were pooled (∼0.5 L), and the pool was concentrated 50-fold by ultrafiltration in an Amicon cell equipped with a YM30 membrane. The protein was dialyzed against 100 mM Na-HEPES buffer, pH 7.6, containing 10% (w/v) glycerol (buffer B), flash-frozen in liquid nitrogen, and stored at −80 °C. Denaturing polyacrylamide gel electrophoresis revealed the protein to be >95% pure. A typical yield was 20 mg/g of cell paste.

The concentration of the apoprotein was determined spectrophotometrically by using the molar absorption coefficient at 280 nm (ϵ_{280}) calculated according to the method of Gill and von Hippel (108.62 mM^{-1} cm^{-1}) (*47*).

Preparation of the Peroxo Intermediate by the Rapid Freeze−*Quench Method.* The protocol for generating rapid freeze−quench Mössbauer samples has been previously described (*11*, *48*). The modifications necessary to generate a dual Mössbauer/EXAFS sample have also been described elsewhere (*17*). An Update Instruments rapid freeze−quench airtight syringe was loaded in a glovebox with a solution made by mixing 2.8 equiv of an anaerobic ^{57}Fe(II) solution [prepared as previously described (*11*)] to an anaerobic sample of R2-W48A/D84E protein in 100 mM HEPES/10% glycerol, pH 7.6, buffer. The opposing RFQ syringe was loaded with O$_2$-saturated 100 mM HEPES/10% glycerol buffer (pH 7.6). The reactants were allowed to reach 5 °C (maintained with a circulating water bath) prior to initiating the reaction by actuation of the ram drive. The reaction was sprayed into −140 °C isopentane after 180 or 213 ms. Typical final protein concentrations after mixing were between 475 and 500 μM. Typical sample volumes were 450 μL.

Control samples of the reactant diiron(II) protein were generated by adding 2.8 equiv of ^{57}Fe(II) to anaerobic 1.47 mM D84E/W48A R2 protein. The sample was added to a Mössbauer/EXAFS sample cell. Approximately 100 mL of isopentane was frozen solid with liquid nitrogen in a shallow glass dewar and was put into the glovebox antechamber. Evacuation of the antechamber caused the isopentane to melt, but its temperature remained sufficiently low to rapidly freeze the samples without the introduction of ice crystals. The frozen samples were transferred to a sealed glass tube to remove them from the glovebox for storage under liquid nitrogen.

Mössbauer Spectroscopy. The Mössbauer spectra were recorded in spectrometers that operate in a constant acceleration mode and that have been described previously (*11*). The zero velocity of the spectra refers to the centroid of a room temperature spectrum of a metallic iron foil. Spectral simulations were performed using the program WMOSS (WEB Research).

XAS Data Collection and Data Analysis. X-ray absorption data were collected at the Stanford Synchrotron Radiation Laboratory (SSRL) primarily on beamline 7-3 but also on beamline 9-3. Samples were maintained at 10 K during data collection using an Oxford Instruments liquid He cryostat. Si(220) monochromator crystals were used at both beamlines. The beamlines were equipped with multielement Canberra germanium detectors (30 elements on 9-3, 13 elements on 7-3) for detection of the iron Kα fluorescence from the samples. Count rates on both beamlines were 2000−3000 cps windowed and ~50000 cps incident. On beamline 7-3, the incident X-ray intensity was detuned by 50% at 8000 eV to reject harmonics. On beamline 9-3, a 10 keV cutoff harmonic rejection mirror allowed the use of fully tuned incident intensity. To reduce the intensity of the incident beam on beamline 9-3, the bend of the focusing mirror was adjusted to make the beam as diffuse as possible. In addition, 6−8 layers of 5 mil Kapton film were placed upstream from the sample. With this experimental setup, the edge energies of samples collected on 9-3 were the same as those collected on beamline 7-3.

Spectra shown here are averages of 20−40 individual, 40 min scans. Scans were defined with 5 eV spacing in the preedge region, a 0.3 eV spacing in the edge region, and 0.05 Å^{-1} spacing in the EXAFS region (2−14 Å^{-1}, k^3-weighted collection time with a maximum of 25 s). Energy calibration was achieved by affixing a small photodiode covered with an iron foil to the front of the 2.5 mm × 3 mm Huber slits that define the beam size prior to the sample. The inflection point of the rising edge of the Fe metal spectrum collected simultaneously was set to be 7111.2 eV. The data presented here are representative of two different diiron(II) control samples and four different samples of the intermediate.

The details of the data analysis procedure have been previously described (*17*). The raw k^3-weighted EXAFS data after spline removal are shown here in k space (Å^{-1}), where k is the photoelectron wavevector defined by

$$k = [(8\pi^2 m_e/h^2)(E - E_0)]^{1/2} \tag{1}$$

E_0 is the threshold energy of excitation of the 1s electron, set initially to 7130 eV. Fits shown here are to Fourier-filtered data, where the EXAFS oscillations in k space have been Fourier transformed to R space (Å) and then the peaks of interest were back-transformed to k space. For ease of visual inspection, the frequency deconvoluted Fourier transforms (FT) of the raw data are also shown. Least-squares fits to the EXAFS oscillations, χ, are evaluated for goodness of fit, F, using eq 2. An additional statistic defined in eq 3,

$$F = [\sum k^6(\chi_{\text{obs}} - \chi_{\text{calc}})^2/N]^{1/2} \tag{2}$$

$$\epsilon' = F^2/\nu \tag{3}$$

ϵ', was used to scale the improvement in goodness of fit as more shells (variables) are added. N_{PTS} is the number of degrees of freedom given by $N_{\text{PTS}} = 2\Delta k\Delta R/\pi$ (*49*). ρ is the number of variable parameters in each fit (R and σ, the mean square deviation in bond length, for each shell of scatterers). ν is defined as $N_{\text{PTS}} - \rho$.

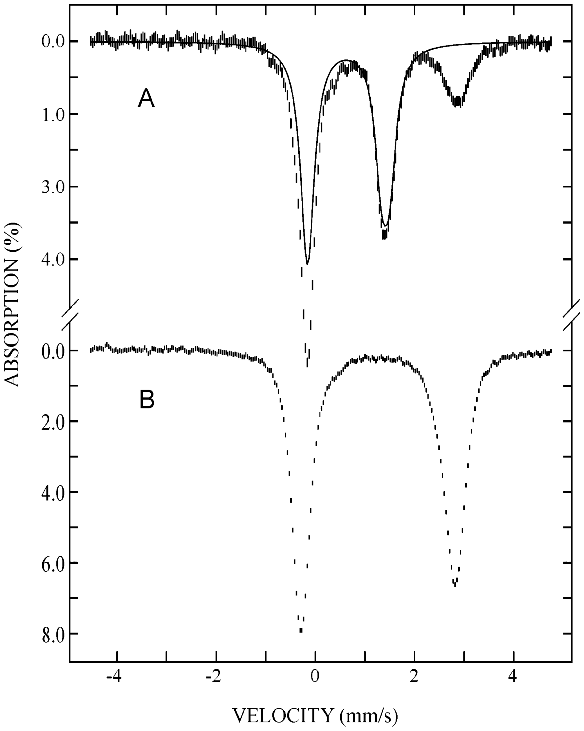

FIGURE 1: Mössbauer spectra of (A) a rapid freeze-quenched sample prepared by reacting R2-W48A/D84E with Fe(II) and O_2 for 180 ms at 5 °C (see Materials and Methods) and (B) a diferrous R2-W48A/D84E sample. These spectra were recorded at 4.2 K in a magnetic field of 50 mT applied parallel to the γ-beam and were acquired prior to XAS data collection. The solid line in (A) is a theoretical spectrum of R2$_{\text{peroxo}}$ simulated with two overlapping equal intensity quadrupole doublets of the following parameters: $\delta(1) = 0.60$ mm/s, $\Delta E_Q(1) = 1.47$ mm/s and $\delta(2) = 0.66$ mm/s, $\Delta E_Q(2) = 1.68$ mm/s. The theoretical spectrum is scaled to 70% of the total absorption area of the experimental spectrum.

RESULTS

Sample Speciation As Determined by Mössbauer Spectroscopy. Mössbauer spectroscopy was used to determine the sample speciation of RFQ XAS samples. The Mössbauer spectra of the peroxodiiron(III) species from MMO, from Δ^9-desaturase, and from R2-D84E variants all share similar spectral features (*27*, *50*, *51*). Like the peroxo species that is formed with R2-D84E (*36*), the diamagnetic peroxo species in R2-W48A/D84E has an isomer shift of $\delta = 0.63$ mm/s and a splitting of $\Delta E_Q = 1.58$ mm/s. Figure 1 is a comparison of the Mössbauer spectra of a sample taken prior to XAS analysis and a control sample of the reactant diiron(II) R2-W48A/D84E. The Mössbauer spectrum of the sample was unchanged after exposure to X-rays during data collection (data not shown). The early quenching time (~200 ms) and the use of substoichiometric Fe (2.8 equiv per R2 dimer) ensure that the freeze-quenched XAS samples contain only the first detectable reaction intermediate, R2$_{\text{peroxo}}$, and the not yet reacted diiron(II) protein. The composition of the XAS samples can be determined by deconvolution of their

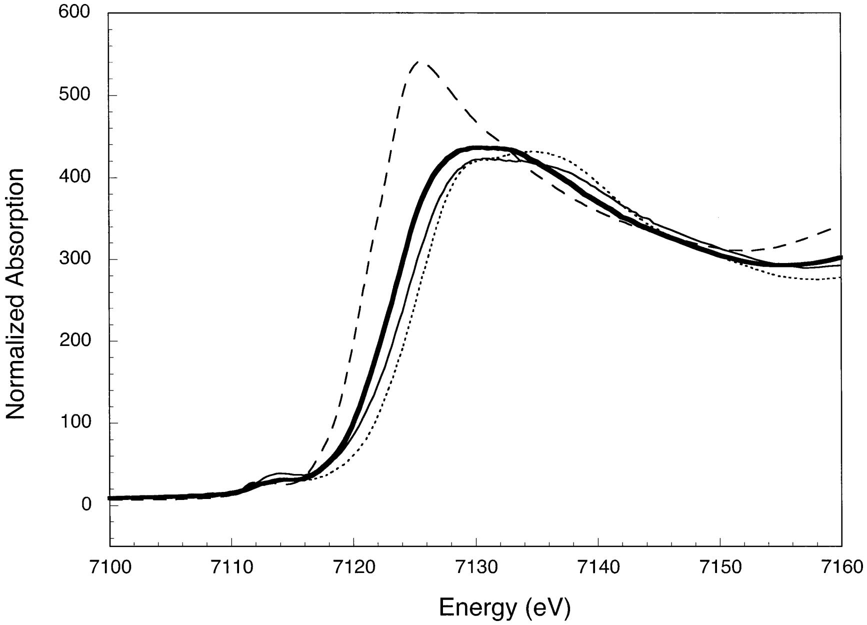

FIGURE 2: X-ray absorption edges from left to right of W48A/D84E diferrous R2 (long dashed line), the RFQ W48A/D84E peroxo sample (70% peroxo/30% diferrous shown as a solid, bold line), the RFQ wild-type X sample (60% X, 40% diferrous shown as a solid line), and D84E diferric control (short dashed line).

Mössbauer spectra into contributions from the reactant and intermediate. Summation of a model spectrum of diiron(II) R2-W48A/D84E (Figure 1B) and the theoretical spectrum of $R2_{peroxo}$ (solid line in Figure 1A) satisfactorily reproduces the experimental spectra. The result indicates that the XAS samples contained 70% $R2_{peroxo}$ and 30% diiron(II) reactant. The quenched peroxo samples were all blue in color from the absorption band at $\lambda_{max} = 700$ nm, a defining feature of this and similar peroxodiiron(III) complexes (*36*).

X-ray Absorption Near Edge Spectra. The X-ray absorption edge energy is indicative of oxidation state. Figure 2 compares the edges of a 100% diiron(II) D84E/W48A sample and a W48A/D84E $R2_{peroxo}$ sample with 70% $R2_{peroxo}$ and 30% diiron(II) reactant. The edge of the $R2_{peroxo}$ sample is higher in energy than that of the diiron(II) control sample but lower in energy than that of a diiron(III) control sample. For an additional comparison, the spectrum of a wild-type sample containing 60% intermediate X and 40% diiron(II) R2 is shown (*17*). The average oxidation state of the Fe in the sample of X is 2.9, and the average oxidation state of the Fe in the peroxo sample is 2.7. The edge energies are consistent with the speciation established by Mössbauer spectroscopy.

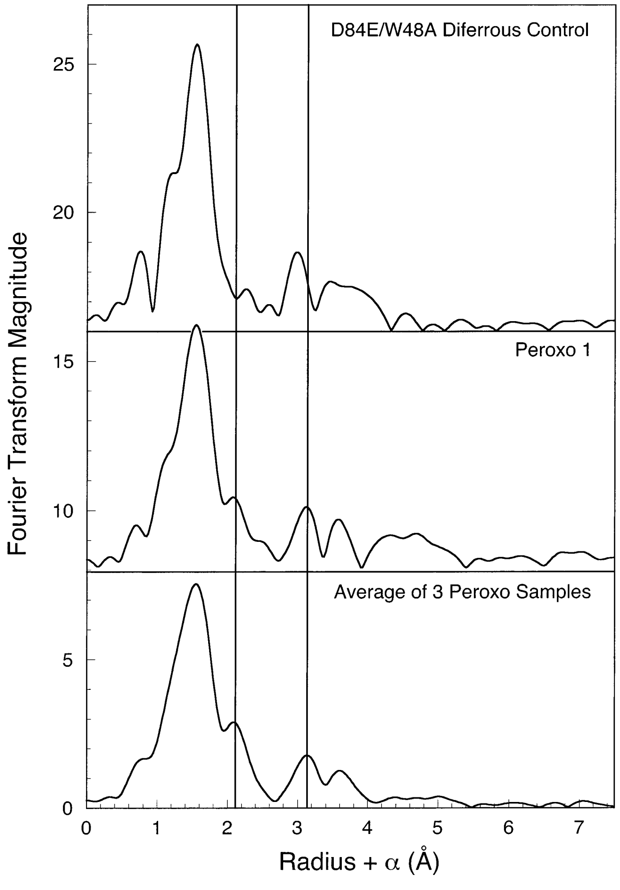

FIGURE 3: Fourier transforms of XAS data of, from top to bottom, (1) D84E/W48A diferrous control, (2) a single data set of a representative RFQ peroxo sample quenched at 180 ms, and (3) the average of three independent data sets of the D84E/W48A peroxo. FTs are offset for clarity. The vertical lines indicate the position of the 2.5 Å Fe−Fe peak ($R + \alpha = 2.1$ Å) and the 3.5 Å Fe−Fe peak ($R + \alpha = 3.1$ Å).

EXAFS Spectra and Fitting Results. Figure 3 shows the Fourier-transformed spectra of diiron(II) R2-W48A/D84E and of a representative RFQ $R2_{peroxo}$ sample with the 70% $R2_{peroxo}$/30% diiron(II) R2 distribution. It also shows the FT data of three $R2_{peroxo}$ samples averaged together. The vertical lines on the graph mark the positions of the two Fe−Fe vectors unique to the $R2_{peroxo}$ samples that were identified in the fitting (vide infra). Both $R2_{peroxo}$ FTs have a feature at $R + \alpha = 2.10$ Å, which corresponds to an actual distance of 2.5 Å (the phase shift, α, is typically −0.4 Å). The second vertical line marks a feature at $R + \alpha = 3.1$ Å ($R = 3.5$ Å). Neither of these features is present in the control sample of the reactant. Instead, the main feature in the second coordination sphere of the diiron(II) control sample is at $R + \alpha = 3.0$ Å ($R = 3.4$ Å). The reduced FT intensity from the first coordination sphere for the sample of the intermediate relative to that for the control sample reflects either the

Table 1: Fitting Results to a Representative R2-W48A/D84E R2$_{\mathrm{peroxo}}$ Sample[a]

	Fe−O			Fe−O			Fe−Fe			Fe−Fe/C			Fe−C					
model	R	CN	σ^2	R	CN	σ^2	R	CN	σ^2	R	CN	σ^2	R	CN	σ^2	F	ϵ'	no.
O, O	2.06	5	11	2.44	1	7.7										0.395	0.0090	1
O, O	1.94	1	4.1	2.08	3	4.5										0.458	0.0121	2
O, Fe	2.06	4	8.8				3.54	0.3	1.4							0.419	0.0101	3
O, Fe	**2.06**	**4**	**9.2**				**2.50**	**0.7**	**11**							**0.379**	**0.0083**	**A**
O, O, Fe	2.06	5	12	2.45	1	4.1	3.56	0.9	10							0.329	0.0070	4
O, O, Fe	1.87	0.5	13	2.07	4	8.5	2.50	0.6	10							0.365	0.0087	5
O, Fe, C	2.06	4	9.2				2.50	0.6	9.8				3.56	2	1.7	0.332	0.0072	6
O, Fe, Fe	**2.06**	**4**	**9.4**				**2.50**	**0.6**	**9.6**	**3.54**	**0.3**	**1.2**				**0.308**	**0.0062**	**B**
O, O, Fe, C	2.06	5	12	3.20	1	9.8	2.49	0.9	13				3.55	2	1.7	0.301	0.0068	7
O, O, C, C	1.88	0.5	10	2.07	4	8.1				2.51	1	2.5	3.56	2	1.8	0.362	0.0098	8
O, O, Fe, Fe	1.87	0.5	12	2.07	4	8.5	2.50	0.7	11	3.54	0.3	1.3				0.281	0.0059	9
O, Fe, Fe, C	**2.06**	**4**	**9.2**				**2.50**	**0.7**	**11**	**3.54**	**0.3**	**1.6**	**4.11**	**3**	**4.1**	**0.215**	**0.0035**	**C**
O, O, Fe, Fe, C	1.88	0.5	10	2.07	4	8.3	2.50	0.9	13	4.10	0.6	7.6	3.56	2	2.1	0.232	0.0047	10
O, O, Fe, Fe, C	1.88	0.5	9.8	2.07	4	7.9	3.54	0.3	1.3	4.10	0.9	10	2.52	1	2.6	0.259	0.0059	11
O, O, Fe, C, C	1.92	0.5	1.4	2.07	3	4.6	2.51	0.3	6.4	3.56	2	2.0	2.97	1	5.0	0.308	0.0083	12
O, O, Fe, C, C	1.87	0.5	11	2.06	4	8.1	3.55	0.6	6.7	2.51	1	1.6	2.97	1	1.4	0.277	0.0067	13
O, O, Fe, Fe, C	**1.87**	**0.5**	**12**	**2.06**	**4**	**8.5**	**2.50**	**0.6**	**10**	**3.53**	**0.3**	**1.6**	**4.11**	**3**	**4.0**	**0.177**	**0.0027**	**D**
O, O, Fe, Fe, C	*1.91*	*0.8*	*6.9*	*2.06*	*3.3*	*6.6*	*2.49*	*0.7*	*8.9*	*3.54*	*0.3*	*4.5*	*4.12*	*2.3*	*3.6*			

[a] Selected fits to Fourier-filtered data ($R + \alpha = 0.85-3.90$ Å); R is the absorber/scatterer distance in Å; σ^2 is in units of Å$^2 \times 10^3$; best fits are in bold; average fit results from different peroxo samples are in italics; fit range = 1−12 Å^{-1}.

Table 2: Fourier-Filtered Fitting Results to a Representative R2-W48A/D84E R2$_{\mathrm{peroxo}}$ Sample[a]

Filtered First Shell Fits (Filter = 0.85−2.70 Å; $N_{\mathrm{PTS}} = 2\Delta k\Delta R/\pi = 12.96$)

	Fe−O			Fe−O			Fe−Fe/C*					
model	R	CN	σ^2	R	CN	σ^2	R	CN	σ^2	F	ϵ'	no.
O	2.06	4	9.0							0.363	0.0120	14
O, O	2.06	5	11.7	2.45	1	4.1				0.214	0.0051	15
O, Fe	2.06	4	9.4				2.50	0.6	9.6	0.186	0.0039	16
O, O	1.95	1	6.1	2.08	3	5.5				0.311	0.0108	17
O, O, Fe	**1.87**	**0.5**	**13.9**	**2.06**	**4**	**8.6**	**2.50**	**0.6**	**9.8**	**0.144**	**0.0030**	**E**

Filtered Second Shell Fits (Filter = 2.70−3.90 Å; $N_{\mathrm{PTS}} = 2\Delta k\Delta R/\pi = 8.40$)

	Fe−Fe/C*			Fe−C*/Fe					
model	R	CN	σ^2	R	CN	σ^2	F	ϵ'	no.
Fe	3.54	0.3	1.8				0.246	0.0095	19
C	4.11*	4	5.9				0.235	0.0086	20
C, Fe	3.56*	2	2.6	4.10	0.7	8.8	0.187	0.0079	21
C, C	3.56*	2	2.5	4.11*	3	3.8	0.141	0.0045	22
Fe, Fe	3.54	0.4	3.6	4.10	0.6	7.6	0.134	0.0041	23
Fe, C	**3.54**	**0.3**	**2.1**	**4.11***	**3**	**4.1**	**0.112**	**0.0029**	**F**

[a] Selected fits to Fourier-filtered data; R is the absorber/scatterer distance in Å; σ^2 is in units of Å$^2 \times 10^3$; an asterisk indicates a carbon fit; best fits are in bold; fit range = 1−12 Å^{-1}.

sample inhomogeneity or the presence of two resolvable subshells in the first coordination sphere.

Table 1 shows the results of the fitting analysis for the data from a representative sample of the intermediate. Similar analyses were obtained with the other R2$_{\mathrm{peroxo}}$ samples. The fits are to Fourier-filtered data where all peaks above the noise level are included in the filter, $R + \alpha = 0.85-3.90$ Å. The same conclusions can be drawn when analyzing fits done with smaller filter ranges to the isolated first shell data ($R + \alpha = 0.85-2.70$ Å) and to the isolated second shell data ($R + \alpha = 2.70-3.90$ Å), shown in Table 2. Table 1 is divided into two-, three-, four-, and five-shell models. The best fit in each model category, as judged by the F value, is shown in bold. These best fits, labeled A, B, C, and D for the two-, three-, four-, and five-shell models, respectively, are compared in Figure 4 to the experimental data. The ϵ' values for fits A−D all indicate a significant improvement in fit as a new shell of scatterers is added to the model. Collectively, the fits in Tables 1 and 2 indicate that five interactions are needed to model the data. As demonstrated by fit D in Table 1, the R2$_{\mathrm{peroxo}}$ EXAFS interactions are Fe−O vectors at 1.87 and 2.06 Å, Fe−Fe vectors at 2.50 and 3.53 Å, and Fe−C vectors at 4.11 Å. The last line in Table 1 tabulates the average value of the best five-shell fit parameters for the different peroxo samples examined.

The primary objective of this work was to define the Fe−Fe distance in the R2$_{\mathrm{peroxo}}$ intermediate. In all samples of the R2-W48A/D84E reaction mix containing predominantly the peroxo complex, Fe−Fe vectors at 2.5 Å and at 3.5 Å could be identified. Modeling either of these interactions with a low-Z ligand such as carbon or oxygen decreases the fit quality. This trend can be seen in Table 1 by comparing fits within the three-, four-, and five-shell models (compare fits 7 and 8 to fit C, for example). In all cases, fits with two Fe−Fe shells best model the data. In Table 2, fits to the first shell also indicate the necessity of an Fe−Fe vector at

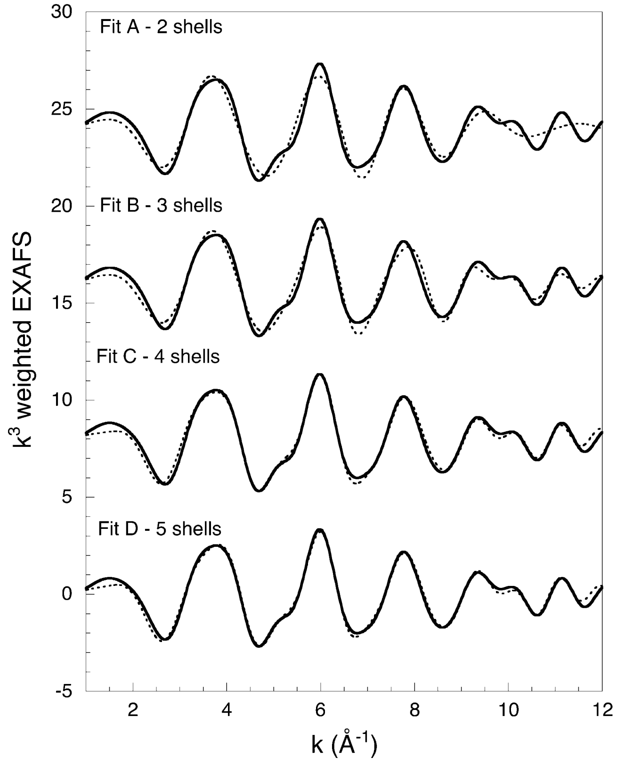

FIGURE 4: Fits to filtered XAS data over the data range $R + \alpha = 0.85-3.90$ Å for a representative peroxo data set. Fits: A, best two-shell model; B, best three-shell model; C, best four-shell model; D, best five-shell model. Fit parameters are given in Table 1. The dashed line is the calculated fit, and the solid line is the Fourier-filtered data. Fits are offset for clarity.

2.5 Å to model the data (compare fit 17 to fit E or fit 15 to fit 16). Likewise, the best fits in the second shell include an Fe−Fe interaction at 3.5 Å (compare fits 20, 21, and 22 to fit F).

It is noteworthy that the average value of σ^2, the mean square deviation in bond length, for the Fe shell at 2.50 Å refines to a fairly large value of 8.9×10^{-3} Å^2. This value of σ^2 suggests substantial static disorder in the 2.5 Å shell. The source of this disorder is most likely the carboxylate ligands of both the peroxodiiron(III) species and the diiron(II) cluster. Crystal structures of diferric R2 indicate that a broad distribution of Fe−O and Fe−C interactions in the range of 2.4−2.7 Å can be expected (*4*, *20*). Similar large σ^2 values were observed when modeling the 2.46 Å Fe−Fe vector in intermediate Q (8.6×10^{-3} Å^2) (*30*), the 2.5 Å Cu−Cu interactions in the Cu$_A$ center of cytochrome oxidase and its related inorganic model complex (8×10^{-3} Å^2) (*52*), the 2.65 Å Fe−Fe vector in the indigo disulfonate oxidized form of the nitrogenase MoFe protein (8×10^{-3} Å^2) (*53*), and the 3.3 Å Ni−Ni interactions in urease (10×10^{-3} Å^2) (*54*). In each of these cases, sample inhomogeneity, site inhomogeneity, or low-Z ligand interferences are thought to contribute to the large disorder.

To help to define the optimal coordination number for the two Fe−Fe interactions, the best five-shell fit as shown in Table 1 was used as a starting point to construct the matrix of *F* values shown in Table 3. For these fits, *R* and σ were allowed to vary while the Fe−oxygen and Fe−carbon coordination numbers were held fixed at the values reported in fit D of Table 1. The coordination numbers of the Fe−Fe shells were then systematically changed from 0.1 to 0.9 for the Fe shells while *R* and σ remained freely adjusting variables. The *F* values shown in bold are fits where the values of the CN at 2.5 Å and the CN at 3.5 Å add to 1. This is the expected total coordination number if all the Fe in the sample is present as Fe−Fe dimers with detectable Fe−Fe vectors. The *F* values shown in italics represent fits where σ^2 refined to unreasonably low or high values. If the total Fe−Fe coordination number is constrained to be 1 (values in bold along the diagonal in Table 3), then the optimal fit requires 0.7 Fe−Fe interactions for the 2.5 Å shell and 0.3 Fe−Fe interactions for the 3.5 Å shell. This was true for most R2$_{\text{peroxo}}$ samples that were examined. These values match exactly the predicted coordination numbers from the Mössbauer quantitation, if one assigns the 2.5 Å interaction to R2$_{\text{peroxo}}$ and the 3.5 Å interaction to the diferrous R2 contaminant. However, Table 3 also shows that for any given column or row, where one of the Fe−Fe coordination numbers is fixed, the best *F* value is at a very shallow minimum. For example, when the coordination number of the 3.5 Å shell is fixed at 0.4, there is very little change in *F* value as the coordination number of the 2.5 Å interaction is varied from 0.5 to 0.8.

Tables 1 and 2 both indicate that optimal fits require a carbon shell at 4.11 Å. Figure 2 shows the FT of data from three different R2$_{\text{peroxo}}$ samples averaged together. In this figure, the noise level is very low, and the peaks corresponding to the 3.5 Å Fe−Fe interaction and the interaction at 4.1 Å are unambiguously above the noise level. Table 2 indicates that fitting the 4.1 Å feature with Fe rather than a shell of carbons reduces the fit quality (compare fits 20 and 22 to fit F). More importantly, a peak at 4.1 Å is also prominent in the FT of the wild-type protein and in those of every R2 variant examined to date by EXAFS (data not shown), including the diiron(II) R2-W48A/D84E (Figure 2). Thus, the 4.1 Å interaction is not unique to the intermediate and may result from imidazole multiple scattering possibly in combination with scattering from distant carboxylate carbons.

In the first coordination sphere, there is a small improvement in fit when a short Fe−O interaction is included in the fits. This short interaction is the least precise when comparing individual R2$_{\text{peroxo}}$ samples. The refined distance varies from 1.87 to 1.93 Å, whereas the other four distances differ by no more than 0.02 Å from one sample to another. The short distance implies that this interaction is associated with R2$_{\text{peroxo}}$, rather than the contaminating reactant. This is a typical distance for the Fe−O distances in the peroxo bridges of the structurally characterized peroxodiiron(III) complexes (*37*, *38*, *55*). The refined coordination numbers of 0.5−1.0 are consistent with this assignment. The average σ^2 value for the peroxo samples examined for this short shell of oxygen is 6.9×10^{-3} Å^2. The size of the σ^2 implies that other short Fe−O vectors from coordinated carboxylate oxygens may be contributing to the uncertainty of this shell. Including the 1.9 Å subshell of oxygens does not affect the refinement of the other distances (compare fits C and D in Table 1). It is noteworthy that very short (≤1.8 Å) Fe−O interactions typical of μ-oxo bridging interactions are not observed in the EXAFS of R2$_{\text{peroxo}}$ samples.

Two samples of diiron(II) R2-W48A/D84E were interrogated as controls for the 30% contaminant present in the R2$_{\text{peroxo}}$ samples. Table 4 summarizes filtered fits to one of

Table 3: Fit Number Dependence on Fe−Fe Coordination Numbers[a]

	CN 2.5								
CN 3.5	0.1	0.2	0.3	0.4	0.5	0.6	0.7	0.8	0.9
0.1	*0.276*	*0.270*	*0.230*	*0.219*	*0.212*	*0.208*	*0.261*	*0.260*	***0.205***
0.2	*0.249*	*0.218*	*0.198*	*0.185*	*0.177*	*0.173*	*0.170*	***0.170***	*0.170*
0.3	*0.252*	0.221	0.201	0.189	0.181	0.177	**0.175**	0.174	0.175
0.4	*0.257*	0.227	0.208	0.196	0.188	**0.184**	0.182	0.181	*0.182*
0.5	*0.262*	0.232	0.214	0.202	**0.195**	0.191	0.189	0.188	*0.189*
0.6	*0.267*	0.238	0.220	**0.209**	0.202	0.198	0.196	0.195	*0.196*
0.7	*0.272*	0.243	**0.226**	0.215	0.208	0.204	0.202	0.202	*0.202*
0.8	*0.276*	**0.248**	0.231	0.221	0.214	0.210	0.208	0.208	*0.208*
0.9	**0.280**	0.253	0.236	0.226	0.219	0.216	0.214	0.214	0.214

[a] *F* values of best fit D from Table 1 when Fe−Fe coordination numbers are systematically varied; values in italics do not have reasonable σ^2 factors; values in bold have a total Fe−Fe coordination number of 1.0.

Table 4: Fitting Results to a Representative Diferrous R2-W48A/D84E Sample[a]

Filtered First Shell Fits (Filter = 0.6−2.4 Å)

	Fe−O			Fe−O*/Fe				
model	*R*	CN	σ^2	*R*	CN	σ^2	*F*	ϵ'
O	2.06	4	7.1				0.399	0.0150
O, Fe	2.07	4	7.2	2.50	0.5	12	0.326	0.0124
O, O	**2.07**	**5**	**9.0**	**2.41***	**1**	**11**	**0.293**	**0.0100**

Filtered Second Shell Fits (Filter = 2.42−4.30 Å)

	Fe−Fe/C*			Fe−C*/Fe				
model	*R*	CN	σ^2	*R*	CN	σ^2	*F*	ϵ'
Fe	3.41	1	7.9				0.341	0.0104
C				3.43*	2	1.0	0.352	0.0111
C, Fe	3.43*	3	3.1	4.14	1	8.6	0.235	0.0060
C, C	3.43*	2	0.6	4.15*	4	4.1	0.228	0.0057
Fe, Fe	3.44	0.6	6.6	4.13	0.6	6.6	0.242	0.0064
Fe, C	**3.41**	**0.7**	**5.0**	**4.15***	**4**	**4.2**	**0.171**	**0.0032**

[a] Selected fits to Fourier-filtered data; *R* is the absorber/scatterer distance in Å; σ^2 is in units of Å^2 × 10^3; an asterisk indicates a carbon or oxygen fit; best fits are in bold. Fit range = 1−12 Å^{-1}.

these samples. There is no clear peak in the FT of the reduced sample (Figure 1) that corresponds to a distance of 2.5 Å. Nonetheless, an attempt was made to model the data with Fe−Fe at 2.5 Å, and as expected, such fits did not best model the data. Instead, a very slight improvement in fit is seen when a shell of longer oxygens at 2.4 Å is added to the 2.07 Å shell of oxygen scatterers. Crystal structures of reduced R2 indicate that 2.4 Å is a typical Fe(II)−O$_{\text{carboxylate}}$ distance (*20*, *24*). In the second coordination sphere, the Fe−Fe vector in the reduced sample refines to a distance of 3.4 Å rather than 3.5 Å. There is also evidence for the shell of low-Z ligands at 4.1 Å.

DISCUSSION

R2$_{peroxo}$ Fe−Fe Distances. The metal−metal distance of a metalloenzyme cluster is crucial information that drastically limits the structures that must be considered. In this study, two different Fe−Fe interactions, at 2.5 and 3.5 Å, were identified in the EXAFS data of a heterogeneous sample containing predominantly the peroxodiiron(III) species, R2$_{\text{peroxo}}$, generated during the reaction of diiron(II) R2-W48A/D84E with oxygen. The speciation of the sample is known from Mössbauer spectroscopy to be limited to the peroxodiiron(III) species (70%) and the diiron(II) reactant complex (30%). On the basis of the arguments outlined below, the most likely scenario is that the 2.5 Å Fe−Fe vector is associated with R2$_{\text{peroxo}}$ and the 3.5 Å feature is associated with a diiron(II) form of R2-W48A/D84E.

Mössbauer spectroscopy has been used extensively to characterize peroxodiiron(III) species and other intermediates in the oxygen activation reactions of diiron proteins. In particular, Mössbauer spectroscopy has been used to characterize the peroxodiiron(III) complexes formed in the oxygen reactions of ferritin, Δ^9-desaturase, methane monooxygenase, and ribonucleotide reductase (*50*). The Mössbauer isomer shifts (δ) of the protein peroxodiiron(III) complexes range from 0.62 to 0.68 mm/s, with the corresponding ΔE_Q values ranging from 1.06 to 1.90 mm/s (*27*, *36*, *51*, *56*). Mössbauer studies on the peroxodiiron(III) complex in Δ^9-desaturase and model complexes indicate that the technique is sensitive enough to detect site inhomogeneities and asymmetries (*38*, *51*, *57*). Thus, it is significant that the Mössbauer data of R2$_{\text{peroxo}}$ indicate the presence of only one type of iron site; this establishes that only one of the Fe−Fe vectors identified in the EXAFS arises from R2$_{\text{peroxo}}$.

The EXAFS of diiron(II) R2-W48A/D84E has only a single Fe−Fe distance at 3.4 Å, which indicates that the Fe−Fe vector at 2.5 Å is unique to R2$_{\text{peroxo}}$. This study is now the fourth to find an Fe−Fe distance of 2.5 Å associated with reactive Fe−oxygen intermediates of diiron carboxylate proteins. Intermediate X has a 2.50 Å Fe−Fe vector (*17*), intermediate Q from MMO has a 2.46 Å Fe−Fe vector (*30*), and the peroxodiiron(III) complex of ferritin has a 2.53 Å Fe−Fe vector (*58*). It is noteworthy that the EXAFS and edges of X and R2$_{\text{peroxo}}$ are substantially different, as it indicates that R2$_{\text{peroxo}}$ does not convert to X in the X-ray beam. A short, 1.79 Å, μ-oxo-bridging interaction is prominent in the EXAFS of X (*17*), whereas the shortest distance in R2$_{\text{peroxo}}$ is 1.9 Å, a distance appropriate for an Fe(III)−O$_{\text{peroxo}}$ interaction (*37*, *38*, *55*). Furthermore, the edge of a sample containing 60% X is higher in energy than the sample containing 70% R2$_{\text{peroxo}}$, also suggesting that the R2$_{\text{peroxo}}$ has not converted to X. The stability of R2$_{\text{peroxo}}$ in the X-ray beam is also demonstrated by the identical Mössbauer spectra prior to and after XAS data collection.

The additional 3.5 Å Fe−Fe feature in the R2$_{\text{peroxo}}$ samples can be assigned to the contaminating diiron(II) R2-W48A/D84E. When the coordination numbers for the two Fe−Fe shells are systematically varied while constraining the overall Fe−Fe coordination number to be equal to 1, the refined values match exactly the quantitation indicated by the Mössbauer analyses. The 2.5 Å CN of 0.7 corresponds to

Scheme 2

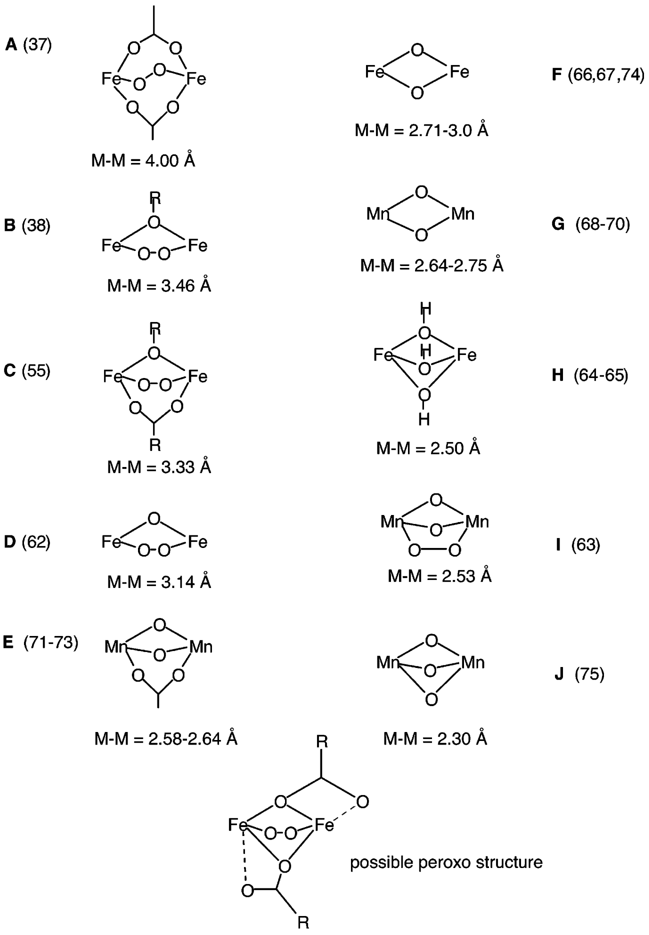

the 70% peroxo species, and the 3.5 Å CN of 0.3 corresponds to the 30% diiron(II) species. The crystal structure of diiron(II) R2-D84E also lends support to this assignment. The Fe−Fe distances of two monomers of dithionite-reduced R2-D84E were reported as 3.44 and 3.53 Å, which matches well with the 3.53 Å Fe−Fe distance observed in the EXAFS (*20*). In this structure of reduced R2-D84E, E238 adopts a μ-(η^1,η^2) bridging mode, E115 adopts a μ-(1,3) bridging mode, and E84 is bidentate to Fe1. The μ-(η^1,η^2)−carboxylate bridge significantly shortens the Fe−Fe vector from the 3.9 Å distance found for the reduced WT protein where both bridges are μ-(1,3) carboxylates (*18*).

The 3.53 Å distance observed in the $R2_{peroxo}$ samples is significantly different from the 3.41 Å Fe−Fe distance found for the reactant control sample. This difference in distances is greater than the often reported and seldom disputed 0.02 Å accuracy of EXAFS distance determinations (*59*). There is an important experimental difference, however, between the unreacted diiron(II) complex in the rapid freeze-quenched $R2_{peroxo}$ sample and the population in the 100% diiron(II) control sample. The control sample was made and frozen entirely in the anaerobic environment of a glovebox. In contrast, the 30% unreacted diiron(II) R2-W48A/D84E in the RFQ sample has been exposed to oxygen in the quenching process but, according to the Mössbauer analysis, has not yet reacted. The exposure to oxygen, then, might explain the differences in distance between pure diiron(II) R2-W48A/D84E (3.41 Å) and the diiron(II) contaminant (3.53 Å). These results may suggest that a noncovalent, O_2-bound intermediate precedes the formation of the peroxo complex. Such a noncovalent complex preceding P in the reaction of MMO with O_2 has been inferred from kinetic evidence (*60*, *61*), but no evidence for a similar complex in the reaction of R2 or any of its variants has yet been reported. Alternatively, multiple forms of the diferrous cluster might be present in solution, and the form with the greater Fe−Fe distance reacts less readily with O_2. The noninteger (0.7) optimal CN for the Fe−Fe shell at 3.4 Å would be consistent with the presence of multiple forms of diiron(II) R2. Experiments are underway to distinguish among these and other possibilities.

Structural Implications. The observation of a 2.5 Å Fe−Fe interaction for the peroxo species places narrow constraints on the structural possibilities for its core. Additional constraints on the core structure have already been reported in a resonance Raman study on the related variant R2-W48F/D84E (*39*). The Raman spectroscopy indicates that the peroxo ligand is bridging and symmetric to the iron ions. Furthermore, the observation of a high O−O stretching frequency of 870 cm^{-1} ruled out a symmetric μ-(η^2,η^2) peroxide bridge. The inorganic model literature provides several examples of structurally characterized peroxodiiron(III) compounds with Fe−Fe distances ranging from 3.1 to 4.0 Å (*37*, *38*, *55*, *62*) (compounds A−D, Scheme 2) and several examples of dinuclear complexes with short metal−metal distances (compounds E−J) (*63*−*75*). Scheme 2 summarizes these structural findings and demonstrates how strongly the metal−metal distance depends on the bridging arrangement. A triply bridged structure with multiple single-atom bridges has thus far been a prerequisite for distances as short as 2.5 Å. These findings and the known propensity of the carboxylate ligands to change coordination modes provide the basis for a proposed core structure of the peroxo intermediate in the reactions of R2-D84E variants shown at the bottom of Scheme 2. Combined with a symmetric peroxo bridge, two μ-(1,1)− or μ-(η^1,η^2)−carboxylate bridges would introduce the single-atom bridges to accommodate a short Fe−Fe distance. The μ-1,2 peroxo, di-μ-oxo dimanganese complex with a 2.53 Å Mn−Mn distance by Bossek et al. provides a synthetic precedent for this structural motif (*63*).

The proposed $R2_{peroxo}$ core structure given in Scheme 2 is the same as the structure proposed by Hwang et al. for the peroxodiiron(III) intermediate of ferritin (*58*). As noted by Hwang et al., if chemically reasonable values for the O−O distance (1.4 Å) and $Fe-O_{peroxo}$ distances (1.9 Å) are combined with the 2.5 Å Fe−Fe constraint, then the Fe−O−O angle of $R2_{peroxo}$ must be close to 107° (*37*, *38*, *55*, *58*). In contrast, the three crystallographically characterized peroxodiiron(III) model complexes have Fe−O−O angles between 118° and 129° (compounds A−C, Scheme 2) (*37*, *38*, *55*). Compound A, $[Fe_2(O_2)(O_2CCH_2C_6H_5)_2\{HB(pz')_3\}_2]$, and compound D, a μ-oxo, μ-(1,2)-peroxo-bridged model, have high O−O stretching frequencies as well (888 and 848 cm^{-1}, respectively) (*37*, *62*), a property shared by the peroxo intermediates of Δ^9-desaturase, ferritin, and R2-D84E (898, 851, and 870 cm^{-1}, respectively) (*76*).

Brunold et al. have concluded that the high O−O stretching frequencies common to both protein and small model peroxodiiron(III) complexes do not reflect strong O−O bonds (*77*). Normal coordinate analyses of resonance Raman profiles of the peroxodiiron(III) complex $[Fe_2(O_2)(OBz)_2\{HB(pz')_3\}_2]$, a compound related to the structurally characterized phenylacetate analogue (compound A), allowed them to instead conclude that the high O−O stretching frequencies result from mechanical coupling of the O−O stretch to the symmetric Fe−O stretch. Brunold et al. then calculated how the O−O frequency depends on the Fe−O−O angle, γ, for a planar Fe−O−O−Fe core. The calculations predict that a 107° Fe−O−O bond angle would give rise to an O−O stretching frequency of about 840 cm^{-1}, somewhat lower than the observed 870 cm^{-1} vibration for $R2_{peroxo}$. It is noteworthy, however, that the ferritin peroxo species and $R2_{peroxo}$ have significantly lower O−O stretching frequencies (851 and 870 cm^{-1}, respectively) (*39*, *78*) than the Δ^9-desaturase peroxo species (898 cm^{-1}) (*26*, *76*). Compound D, $[Fe_2(\mu\text{-}O)(O_2)(6\text{-}Me_3\text{-}TPA)_2](ClO_4)_2]$, a peroxodiiron(III) complex with an additional μ-oxo bridge, also has a lower O−O stretching frequency (848 cm^{-1}) (*62*). Compound A with no single-atom bridges has an O−O frequency more similar to that of the Δ^9-desaturase intermediate, 888 cm^{-1} (*37*). It appears, then, to be generally true that the shorter Fe−Fe distances and the associated smaller Fe−O−O angles lead to lower O−O frequencies from diminished mechanical coupling, as predicted by Brunold et al.

A comparison of the O−O stretching frequencies from $[Fe_2(O_2)(OBz)_2\{HB(pz')_3\}_2]$ (876 cm^{-1}) and $[Fe_2(O_2)(O_2CCH_2C_6H_5)_2\{HB(pz')_3\}_2]$ (888 cm^{-1}), however, suggests that very subtle electronic changes can also alter O−O frequencies, without necessarily leading to a change in Fe−O−O angle (*79*). At present, compound A, $[Fe_2(O_2)(O_2CCH_2C_6H_5)_2\{HB(pz')_3\}_2]$, remains the only crystallographically characterized model complex where the O−O stretching frequency has been determined. This lack of structural and spectroscopic models makes it difficult to interpret the apparent discrepancy in the Fe−O−O angle predicted for $R2_{peroxo}$ by the analysis of Brunold et al. and its known O−O stretching frequency and the angle dictated by the short Fe−Fe distance. More comprehensive spectroscopic data on both protein complexes and inorganic models are necessary to understand the structural and electronic subtleties that determine chemical reactivity. It is clear, however, that common to all of the oxygen activation reactions of dinuclear Fe proteins is the "geometric variability at the dinuclear active site" (*80*). It is most likely the movement of these carboxylates to μ-1,1 or μ-(η^1,η^2) bridging modes that leads to short Fe−Fe distances in four different reactive intermediates, the peroxodiiron(III) complex of ferritin, X, Q, and now the $R2_{peroxo}$ in variants containing the D84E substitution (*17*, *30*, *58*).

REFERENCES

1. Stubbe, J., and van der Donk, W. A. (1995) *Chem. Biol. 2*, 793−801.
2. Reichard, P. (1993) *Science 260*, 1773−1777.
3. Larsson, A., and Sjöberg, B.-M. (1986) *EMBO J. 5*, 2037−2040.
4. Nordlund, P., and Eklund, H. (1993) *J. Mol. Biol 232*, 123−164.
5. Stubbe, J. (1990) *Nature 370*, 502.
6. Ekberg, M., Sahlin, M., Eriksson, M., and Sjöberg, B.-M. (1996) *J. Biol. Chem. 34*, 20655−20659.
7. Stubbe, J. (1990) *J. Biol. Chem. 265*, 5329−5332.
8. Stubbe, J., Nocera, D. G., Yee, C. S., and Chang, M. (2003) *Chem. Rev. 103*, 2167−2201.
9. Atkin, C. L., Thelander, L., Reichard, P., and Lang, G. (1973) *J. Biol. Chem. 248*, 7464−7472.
10. Bollinger, J. M., Jr., Edmondson, D. E., Huynh, B. H., Filley, J., Norton, J. R., and Stubbe, J. (1991) *Science 253*, 292−298.
11. Ravi, N., Bollinger, J. M., Jr., Huynh, B. H., Stubbe, J., and Edmondson, D. E. (1994) *J. Am. Chem. Soc. 116*, 8007−8014.
12. Willems, J.-P., Lee, H. I., Burdi, D., Doan, P. E., Stubbe, J., and Hoffman, B. M. (1997) *J. Am. Chem. Soc. 119*, 9816−9824.
13. Burdi, D., Willems, J.-P., Riggs-Gelasco, P. J., Antholine, W. E., Stubbe, J., and Hoffman, B. M. (1998) *J. Am. Chem. Soc. 120*, 12910−12919.
14. Sturgeon, B. E., Burdi, D., Chen, S., Huynh, B. H., Edmondson, D. E., Stubbe, J., and Hoffman, B. M. (1996) *J. Am. Chem. Soc. 118*, 7551−7557.
15. Burdi, D., Sturgeon, B. E., Tong, W. H., Stubbe, J., and Hoffman, B. M. (1996) *J. Am. Chem. Soc. 118*, 281−282.
16. Bollinger, J. M., Jr., Stubbe, J., Huynh, B. H., and Edmondson, D. E. (1991) *J. Am. Chem. Soc 113*, 6289−6291.
17. Riggs-Gelasco, P. J., Shu, L., Chen, S., Burdi, D., Huynh, B. H., Que, L., Jr., and Stubbe, J. (1998) *J. Am. Chem. Soc. 120*, 849−860.
18. Logan, D. T., Su, X.-D., Åberg, A., Regnström, K., Hajdu, J., Eklund, H., and Nordlund, P. (1996) *Structure 4*, 1053−1064.
19. Rardin, R. L., Tolman, W. B., and Lippard, S. J. (1991) *New J. Chem. 15*, 417−430.
20. Voegtli, W. C., Khidekel, N., Baldwin, J., Ley, B., Bollinger, J. M., Jr., and Rosenzweig, A. C. (2000) *J. Am. Chem. Soc. 122*, 3255−3261.
21. Dunietz, B., Beachy, M., Cao, Y., Whittington, D. A., Lippard, S. J., and Friesner, R. A. (2000) *J. Am. Chem. Soc. 122*, 2828−2839.
22. Rosenzweig, A. C., Nordlund, P., Takahara, P. M., Frederick, C. A., and Lippard, S. J. (1995) *Chem. Biol. 2*, 409−418.
23. Nordlund, P., Sjöberg, B.-M., and Eklund, H. (1990) *Nature 345*, 593−598.
24. Voegtli, W. C., Baldwin, J., Saleh, L., Bollinger, J. M., Jr., and Rosenzweig, A. C. (2003) *J. Am. Chem. Soc.* (in press).
25. Andersson, M. E., Högbom, M., Rinaldo-Matthis, A., Andersson, K. K., Sjöberg, B.-M., and Nordlund, P. (1999) *J. Am. Chem. Soc. 121*, 2346−2352.
26. Liu, K. E., Valentine, A. M., Qui, D., Edmondson, D. E., Appelman, E. H., Spiro, T. G., and Lippard, S. J. (1995) *J. Am. Chem. Soc. 117*, 4997−4998.
27. Liu, K. E., Valentine, A. M., Wang, D., Huynh, B. H., Edmondson, D. E., Salifoglou, A., and Lippard, S. J. (1995) *J. Am. Chem. Soc. 117*, 10174−10185.
28. Wallar, B. J., and Lipscomb, J. D. (1996) *Chem. Rev. 96*, 2625−2657.
29. Feig, A. L., and Lippard, S. J. (1994) *Chem. Rev. 94*, 759−805.
30. Shu, L., Nesheim, J. C., Kauffmann, K. E., Münck, E., Lipscomb, J. D., and Que, L., Jr. (1997) *Science 275*, 515−518.
31. Valentine, A. M., Tavares, P., Pereira, A. S., Davydov, R., Krebs, C., Hoffman, B. M., Edmondson, D. E., Huynh, B. H., and Lippard, S. J. (1998) *J. Am. Chem. Soc. 120*, 2190−2191.
32. Nordlund, P., and Eklund, H. (1995) *Curr. Opin. Struct. Biol. 5*, 758−766.
33. Que, L., Jr., and Dong, Y. (1996) *Acc. Chem. Res. 29*, 190−196.
34. Tong, W. H., Chen, S., Lloyd, S. G., Edmondson, D. E., Huynh, B. H., and Stubbe, J. (1996) *J. Am. Chem. Soc. 118*, 2107−2108.
35. Baldwin, J., Krebs, C., Ley, B. A., Edmondson, D. E., Huynh, B. H., and Bollinger, J. M., Jr. (2000) *J. Am. Chem. Soc. 122*, 12195.
36. Bollinger, J. M., Jr., Krebs, C., Vicol, A., Chen, S., Ley, B. A., Edmondson, D. E., and Huynh, B. H. (1998) *J. Am. Chem. Soc. 120*, 1094−1095.
37. Kim, K., and Lippard, S. J. (1996) *J. Am. Chem. Soc. 118*, 4914−4915.
38. Ookubo, T., Sugimoto, H., Nagayama, T., Masuda, H., Sato, T., Tanaka, K., Maeda, Y., Okawa, H., Hayahi, Y., Uehara, A., and Suzuki, M. (1996) *J. Am. Chem. Soc. 118*, 701−702.
39. Moënne-Loccoz, P., Baldwin, J., Ley, B. A., Loehr, T. M., and Bollinger, J. M., Jr. (1998) *Biochemistry 37*, 14659−14663.
40. Baldwin, J., Voegtli, W. C., Khidekel, N., Moënne-Loccoz, P., Krebs, C., Pereira, A. S., Ley, B. A., Huynh, B. H., Loehr, T. M., Riggs-Gelasco, P. J., Rosenzweig, A. C., and Bollinger, J. M., Jr. (2001) *J. Am. Chem. Soc. 123*, 7017−7030.
41. Krebs, C., Chen, S., Baldwin, J., Ley, B. A., Patel, U., Edmondson, D. E., Huynh, B. H., and Bollinger, J. M., Jr. (2000) *J. Am. Chem. Soc. 122*, 12207−12219.
42. Bollinger, J. M., Jr., Chen, S., Parkin, S. E., Mangravite, L. M., Ley, B. A., Edmondson, D. E., and Huynh, B. H. (1997) *J. Am. Chem. Soc. 119*, 5976−5977.
43. Ochiai, E., Mann, G. J., Gräslund, A., and Thelander, L. (1990) *J. Biol. Chem 265*, 15758−15761.

44. Parkin, S. E., Chen, S., Ley, B. A., Mangravite, L., Edmondson, D. E., Huynh, B. H., and Bollinger, J. M., Jr. (1998) *Biochemistry 37*, 1124−1130.
45. Salowe, S. P., and Stubbe, J. (1986) *J. Bacteriol. 165*, 363−366.
46. Bollinger, J. M., Jr., Tong, W. H., Ravi, N., Huynh, B. H., Edmondson, D. E., and Stubbe, J. (1994) *J. Am. Chem. Soc 116*, 8024−8032.
47. Gill, S., and Von Hippel, P. H. (1989) *Anal. Biochem. 182*, 319−326.
48. Bollinger, J. M., Jr., Tong, W. H., Ravi, N., Huynh, B. H., Edmondson, D. E., and Stubbe, J. (1995) in *Methods in Enzymology* (Klinman, J., Ed.) Academic Press, New York.
49. Lytle, F. W., Sayers, D. E., and Stern, E. A. (1989) *Phys. B 158*, 701−722.
50. Krebs, C., and Huynh, B. H. (1999) *Iron Metabolism*, 253−273.
51. Broadwater, J., Achim, C., Münck, E., and Fox, B. G. (1999) *Biochemistry 38*, 12197−12204.
52. Blackburn, N. J., Barr, M. E., Woodruff, W. H., van der Ooost, J., and de Vries, S. (1994) *Biochemistry 33*, 10401−10407.
53. Christiansen, J., Tittsworth, R. C., Hales, B. J., and Cramer, S. P. (1995) *J. Am. Chem. Soc. 117*, 10017−10024.
54. Wang, S., Lee, M. H., Hausinger, R. P., Clark, P., Wilcox, D., and Scott, R. A. (1999) *Inorg. Chem. 33*, 1589−1593.
55. Dong, Y., Yan, S., Young, V., Jr., and Que, L., Jr. (1996) *Angew. Chem., Int. Ed. Engl. 35*, 618−620.
56. Pereira, A. S., Small, W., Krebs, C., Tavares, P., Edmondson, D. E., Theil, E. C., and Huynh, B. H. (1998) *Biochemistry 37*, 9781−9876.
57. LeCloux, D. D., Barrios, A. M., Mizoguchi, T. J., and Lippard, S. J. (1998) *J. Am. Chem. Soc. 120*, 9001−9014.
58. Hwang, J., Krebs, C., Huynh, B. H., Edmondson, D. E., Theil, E. C., and Penner-Hahn, J. E. (2000) *Science*, 122−125.
59. George, G. N., Hedman, B., and Hodgson, K. O. (1998) *Nat. Struct. Biol. 5*, 645−647.
60. Pulver, S., Froland, W. A., Fox, B. G., and Lipscomb, J. D. (1993) *J. Am. Chem. Soc. 115*, 12409−12422.
61. Valentine, A. M., Stahl, S. S., and Lippard, S. J. (1999) *J. Am. Chem. Soc. 121*, 3876−3887.
62. Dong, Y., Zang, Y., Shu, L., Wilkinson, L., and Que, L. (1997) *J. Am. Chem. Soc. 119*, 12683−12684.
63. Bossek, U., Weyhermüller, T., Wieghardt, K., Nuber, B., and Weiss, J. (1990) *J. Am. Chem. Soc. 112*, 6387.
64. Drüeke, S., Chaudhuri, P., Pohl, K., Wieghardt, K., Ding, X.-Q., Bill, E., Sawaryn, A., Trautwein, A. X., Winkler, H., and Gurman, S. J. (1989) *J. Chem. Soc., Chem. Commun.*, 59−62.
65. Gamelin, D. R., Bominaar, E. L., Kirk, M. L., Wieghardt, K., and Solomon, E. I. (1996) *J. Am. Chem. Soc. 118*, 8085−8097.
66. Dong, Y., Fujii, H., Hendrich, M. P., Leising, R. A., Pan, G., Randall, C. R., Wilkinson, E. C., Zang, Y., Que, L., Jr., Fox, B. G., Kauffmann, K. E., and Münck, E. (1995) *J. Am. Chem. Soc. 117*, 2778−2792.
67. Dong, Y., Que, L., Jr., Kauffmann, K. E., and Münck, E. (1995) *J. Am. Chem. Soc. 117*, 11377−11378.
68. Gohdes, J. W., and Armstrong, W. H. (1992) *Inorg. Chem. 31*, 368−373.
69. Larson, E. J., and Pecoraro, V. L. (1991) *J. Am. Chem. Soc. 113*, 3810−3818.
70. Plaskin, P. M., Stoufer, R. C., Mathew, M., and Palemik, G. J. (1972) *J. Am. Chem. Soc. 94*, 2121.
71. Haselhorst, G., and Wieghardt, K. (1995) *J. Inorg. Biochem. 59*, 624.
72. Pal, S., Chan, M. K., and Armstrong, W. H. (1992) *J. Am. Chem. Soc. 114*, 6398−6406.
73. Dave, B. C., Czernuszewicz, R. S., Bond, M. R., and Carrano, C. J. (1993) *Inorg. Chem. 32*, 3593−3594.
74. Zang, Y., Pan, G., Que, L., Jr., Fox, B. G., and Münck, E. (1994) *J. Am. Chem. Soc. 116*, 3653−3654.
75. Wieghardt, K., Bossek, U., Nuber, B., Weiss, J., Bonvoisin, J., Corbella, M., Vitols, S. E., and Girerd, J. J. (1988) *J. Am. Chem. Soc. 110*, 7398−7411.
76. Broadwater, J., Ai, J., Loehr, T. M., Sanders-Loehr, J., and Fox, B. G. (1998) *Biochemistry 37*, 14664−14671.
77. Brunold, T. C., Tamura, N., Kitajima, N., Moro-oka, Y., and Solomon, E. I. (1998) *J. Am. Chem. Soc. 120*, 5674.
78. Moënne-Loccoz, P., Krebs, C., Herlihy, K., Edmondson, D. E., Theil, E. C., Huynh, B. H., and Loehr, T. M. (1999) *Biochemistry 38*, 5290−5295.
79. Kitajima, N., Tamura, N., Amagai, H., Fukui, H., Moro-oka, Y., Mizutani, Y., Kitagawa, T., Mathur, R., Heerwegh, K., Reed, C. A., Randall, C. R., Que, L., Jr., and Tatsumi, K. (1994) *J. Am. Chem. Soc. 116*, 9071−9085.
80. Whittington, D. A., and Lippard, S. J. (2001) *J. Am. Chem. Soc. 123*, 827−838.

BI035198P